

Chapter - 6

Synthesis and Photoluminescence studies Of undoped, single doped and double doped Strontium Gadolinium Tantalum Oxide

6.1 Introduction

Pervoskites have the common formula ABX_3 , where A and B are two cations of different sizes, and X is an anion that form bonds with both cations [1]. X is usually oxygen, but also other large anions such as halides, sulphides, and nitrides are possible. The pervoskite structures are exists in different form such as: ABO_3 -pervoskite (ex: $BaTiO_3$, $CaTiO_3$), A_2BO_4 -Layered pervoskite (ex: Sr_2RuO_4 , K_2NiF_4), $A_2BB'O_6$ -Double pervoskite (ex: Ba_2TiRuO_6) and $A_2A'B_2B'O_9$ -Triple pervoskite (ex: $La_2SrCo_2FeO_9$), etc [2 - 4].

Number of pervoskite-type oxides have been studied due to their attractive features like superconductivity [5], insulator-metal transition [6], ionic conduction characteristics [7], dielectric properties and ferroelectricity [8]. Pervoskites are one of the most often found structures in solid-state physics, and it carries most of the metal ions of the periodic table with a vital number of different anion.

Through the past few years, many experimental and theoretical researches were dedicated to the study of pervoskite solids. Pervoskite solids are recently gaining more importance in the field of electrical ceramics [9], geophysics[10], material science [11], astrophysics [12], particle accelerators [13], fission-fusion reactors [14, 15], heterogeneous catalysis [16], environment [17], etc.

These types of oxides can accept substitutions in one or both cationic sites (i.e., A and B sites) while retaining their original crystal structures. This kind of feature provides the chemical tailoring of the substances, via partial replacement of the cationic site(s) with foreign metal ions, hence transforming their structural, microstructural, electrical and magnetic properties [18 – 20]. Pervoskite-type oxides have been found many applications in physics and chemistry.

Pervoskite-type structures have specific features due to their nonstoichiometry of the cations and the anions, the distortion of cation configuration, and the valence mixture electronic structure. Most of the metallic elements in the periodic table are stable in a pervoskite-type oxide structure. Therefore the possibility of synthesizing multicomponent pervoskites by partial substitution of cations in positions of A and B gives rise to various complex types.

Ceramics with double-pervoskite structure of general formula $A_2B'B''O_6$ have attracted a great attention due to their rich and challenging physical properties [21] and their potential application in technology. Among the various kinds of double-

pervoskites, $\text{Sr}_2\text{LnTaO}_6$ (Ln = lanthanides) compounds with an ordered arrangement of the Ln and Ta ions at B-site have been investigated by many researchers [22]. Practically all kinds of optical centres study has been carried out in the pervoskite structure for low as well as in high concentration. The optical studies on pervoskite systems have contributed considerably to the development of many optical materials like LASER materials, solar energy conversion, and many more [23]. Although, the permittivity measurement at microwave frequencies of many tantlates have been performed by other researchers [24]. There is no reported data on luminescence properties of rare earth doped $\text{Sr}_2\text{GdTaO}_6$.

In current years, pervoskites gets significant concern in materials research for its laser application. Recently, more researches were focused on luminescent characteristics of rare-earth ions doped pervoskite-type oxides. Pervoskite-type phosphors are very stable and can steadily work in diverse conditions [25, 26].

Moreover, Pervoskite type phosphors are likely candidates in field emission display (FED) and plasma display panel (PDP) devices because they are sufficiently conductive to release electric charges stored on the phosphor particle surfaces [27]. Eu^{+3} is a good activator ion with red or red-orange emission in many hosts, such as borates [28], niobates [29], and molybdates [30]. The PL feature makes pervoskite material assuring for applications such as field emission displays, plasma displays, solid-state lighting, green photocatalyst, and scintillators [31, 32].

6.2 Synthesis and Characterization

6.2.1 Synthesis

The $\text{Sr}_2\text{GdTaO}_6$, $\text{Sr}_2\text{GdTaO}_6: \text{Eu}^{+3}$, $\text{Sr}_2\text{GdTaO}_6: \text{Er}^{+3}$, and $\text{Sr}_2\text{GdTaO}_6: \text{Eu}(1\%)$, $\text{Er}(x\%)$ (Where $x = 0.5, 1.0, 1.5, 2.0$) phosphors were synthesized by combustion synthesis method. The reagents used for this purpose are SrCO_3 (99.9%), Gd_2O_3 (99.9%), Ta_2O_5 (99.9%), Eu_2O_3 (99.9%), Er_2O_3 (99.9%), and Urea (99%) as a flux. These materials were intimately mixed in the stoichiometric ratio corresponding to the nominal composition of all above phosphor and transfer it in alumina crucible and heated at 900°C in muffle furnace for 3 hours, then allowed to cool to room temperature naturally. The synthesized material was grinded in mortar pastel to make the fine powder and final powder product obtained in white color.

6.2.2 Characterization

XRD analyses were done through D8 Bruker advance X-ray Diffractometer, with the Cu K α radiation having ($\lambda = 1.5406 \text{ \AA}$) 40kV voltage, 40mA current, and energy 8.05keV at room temperature by step scanning in range of an angle $20^\circ \leq 2\theta \leq 60^\circ$ with increments of $0.02^\circ/\text{s}$. FTIR spectra registered on a Jasco FTIR- 4100, spectrophotometer (Japan) from the 1mm KBr pallet formed by mixing phosphor with KBr in mortar and pestle in the ratio of 1:100. The photoluminescence (PL) of the samples investigated using the Shimadzu spectrofluorophotometer (5103 R-PC) at room temperature with a xenon lamp as an excitation source for various excitation wavelengths.

6.3 Results and Discussion

6.3.1 X-Ray Diffraction

Figure 6.1 exhibits the powder X-ray diffraction pattern of undoped, single doped, and Eu(III), Er (III) double doped $\text{Sr}_2\text{GdTaO}_6$. The recorded patterns present sharp and well-defined peaks, indicating that the as prepared materials have a highly crystalline nature. There is a good agreement between the observed and calculated interplanar spacing (d-values) that suggest, the compound has a monoclinic phase with a $P2_1/n$ (#14) space group. The relative coordinates and occupancy of each site for $\text{Sr}_2\text{GdTaO}_6$ are mentioned in Table 6.1. The values for the bond distances of cations (relative to the oxygen anion) and occupancy were obtained from the Rietveld refinement which is summarized in Table 6.2. These diffraction lines are consistent and confirm the formation of a double perovskite structure for all studied samples. The average crystallite sizes were estimated by the Scherrer's equation using the full width at half maximum (FWHM) of all hkl marked intense peak. The average crystallite size calculated using the Debye-Scherrer formula [33], which is given as equation (6.1),

$$D = \frac{k \cdot \lambda}{\beta \cdot \cos\theta} \text{ ----- (6.1)}$$

Where, D is the average crystallite size, k is the constant equal to 0.94, λ is the wavelength of the X-rays equal to 0.1542 nm, θ is the Bragg angle and β is FWHM.

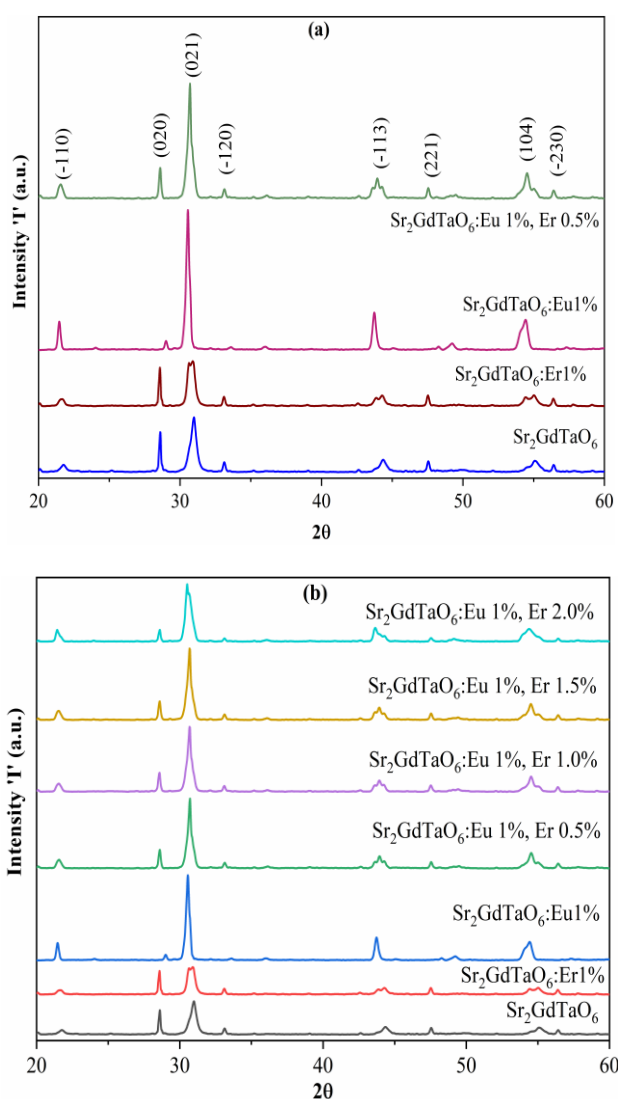


Figure 6.1 Powder X-ray diffraction pattern of (a) undoped, single doped, double doped $\text{Sr}_2\text{GdTaO}_6$ and (b) Eu(III), Er(III) double doped $\text{Sr}_2\text{GdTaO}_6$.

Atom	Site	x	Y	Z
Sr	4e	0.5213	0.5612	0.2475
Gd	2c	0.0000	0.5000	0.0000
Ta	2d	0.5000	0.0000	0.5000
O	4e	0.2222	0.1840	0.0495
O	4e	0.3212	0.7243	0.0496
O	4e	0.4010	0.0167	0.2291

Table 6.1 Structural parameters of $\text{Sr}_2\text{GdTaO}_6$ found by Rietveld analysis of XRD data.

All the reflection peaks of the X-ray profile indexed and lattice parameters are determined with the help of a standard computer program Powder-X. In double perovskite oxide the analysis of distortion from the ideal cubic perovskite structure is clear because the $\text{Sr}_2\text{GdTaO}_6$ complex perovskite has the general formula $\text{A}_2\text{BB}'\text{O}_6$. The tolerance factor T_f of the sample is calculated by using equation (6.2),

$$T_f = \frac{R_{\text{Sr}} + R_{\text{O}}}{\sqrt{2} \left(\frac{R_{\text{Gd}} + R_{\text{Ta}} + R_{\text{O}}}{2} \right)} \text{----- (6.2)}$$

Where, R_{Sr} , R_{Gd} , R_{Ta} and R_{O} are the ionic radii of Sr, Gd, Ta and O respectively [34]. If tolerance factor T_f is equal to unity, there is ideal cubic perovskite structure, and if $T_f < 1$ the structure is distorted from the cubic symmetry, and in accordance with the SPuDs prediction [35], the value of tolerance factor by $\text{Sr}_2\text{GdTaO}_6$ complex perovskite is 0.9135. The malformation from the ideal cubic perovskite the structure is an outcome of the inclination of the $\text{Gd-O}_{6/2}$ and $\text{Ta-O}_{6/2}$ octahedra; in the meantime support their corner connectivity. Then, the Ta^{5+} and Gd^{3+} cations occupy two crystallographic independent octahedral sites, namely 2d and 2c [36]. The crystallographic results of all prepared perovskite are in accordance with other reports, but there is no an enhanced characterization about atomic positions and inter-atomic distances [37].

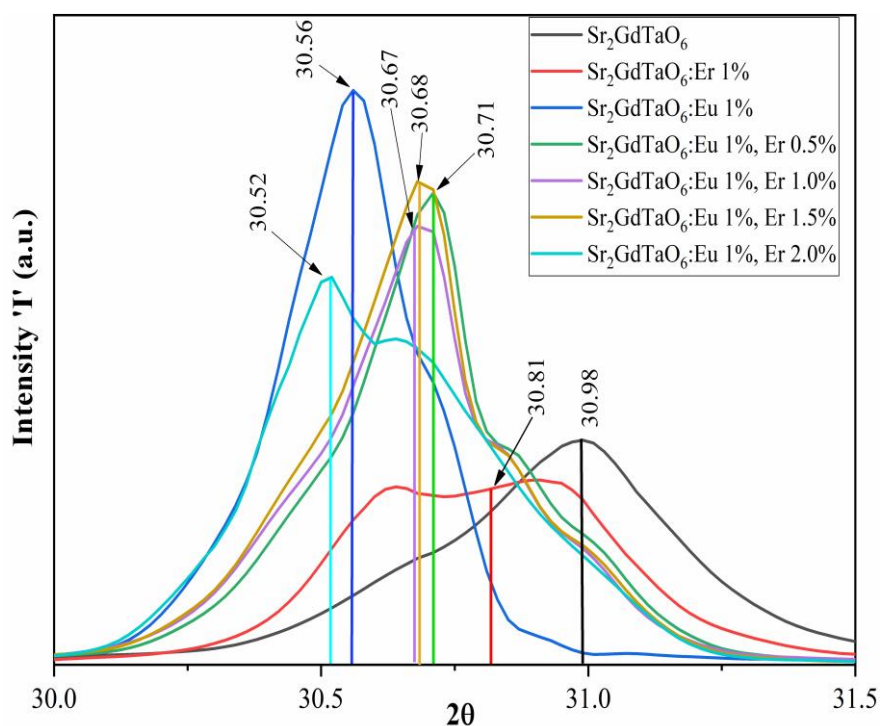


Figure 6.2 Magnified (021) reflection peak of undoped, single doped and Eu(III), Er(III) double doped $\text{Sr}_2\text{GdTaO}_6$.

Cation	Anion & Multi.	Distance (Å)	Occupancy
Gd (2c)	O (4e) X 2	2.3202	1.00
Gd (2c)	O (4e) X 2	2.3228	1.00
Gd (2c)	O (4e) X 2	2.3214	1.00
Ta (2d)	O (4e) X 2	1.9864	1.00
Ta (2d)	O (4e) X 2	1.9885	1.00
Ta (2d)	O (4e) X 2	1.9865	1.00
Sr (4e)	O (4e) X 1	3.7611	1.00
Sr (4e)	O (4e) X 1	2.9630	1.00
Sr (4e)	O (4e) X 1	2.6842	1.00
Sr (4e)	O (4e) X 1	2.5170	1.00
Sr (4e)	O (4e) X 1	2.8913	1.00
Sr (4e)	O (4e) X 1	3.7725	1.00
Sr (4e)	O (4e) X 1	2.5378	1.00
Sr (4e)	O (4e) X 1	2.7338	1.00
Sr (4e)	O (4e) X 1	3.3674	1.00
Sr (4e)	O (4e) X 1	2.4848	1.00
Sr (4e)	O (4e) X 1	3.5312	1.00
Sr (4e)	O (4e) X 1	2.6239	1.00

Table 6.2 Inter-atomic distance and occupancy calculated through Rietveld refinement of experimental data.

From Bragg's equation, the variation in position of reflection peaks implies the change in the lattice parameter of synthesized phosphors [33, 38]. To confirm the change in reflection peaks, the magnified scale of characteristic reflection peak (021) of all $\text{Sr}_2\text{GdTaO}_6$ samples as seen in Figure 6.2 and compare the shift in reflecting angle with the calculated lattice parameters mentioned in Table 6.3. From Figure 6.2, the change in position of the peaks suggests a change in crystallite size and lattice parameter can be seen in the Table 6.3. Due to small crystallite size, the number of parallel planes available is too small for a sharp diffraction maximum to build up and hence the reflection peaks in the diffraction pattern become broadened for all samples (Figure 6.2) [39].

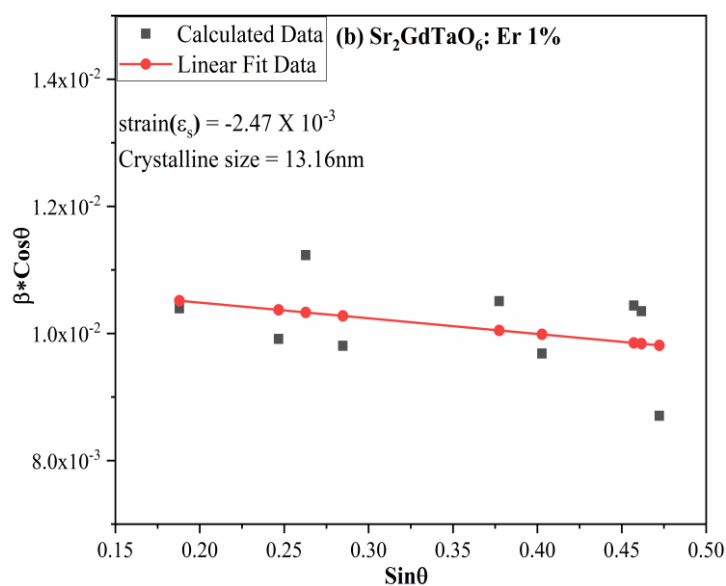
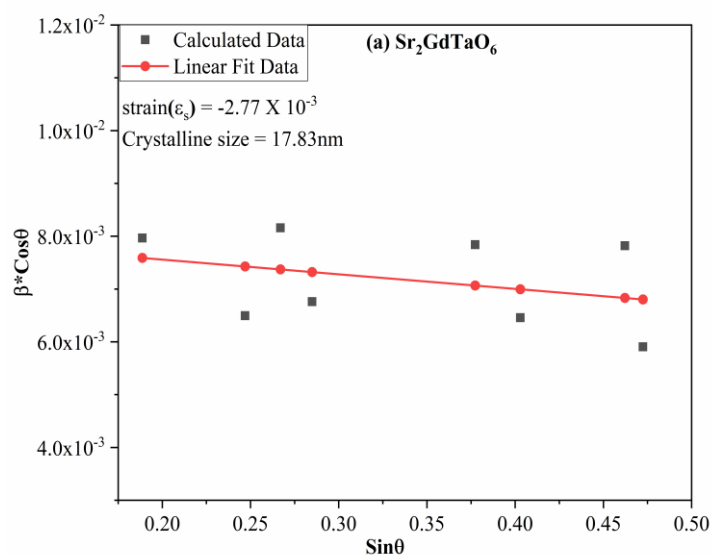
Williamson-Hall Plot

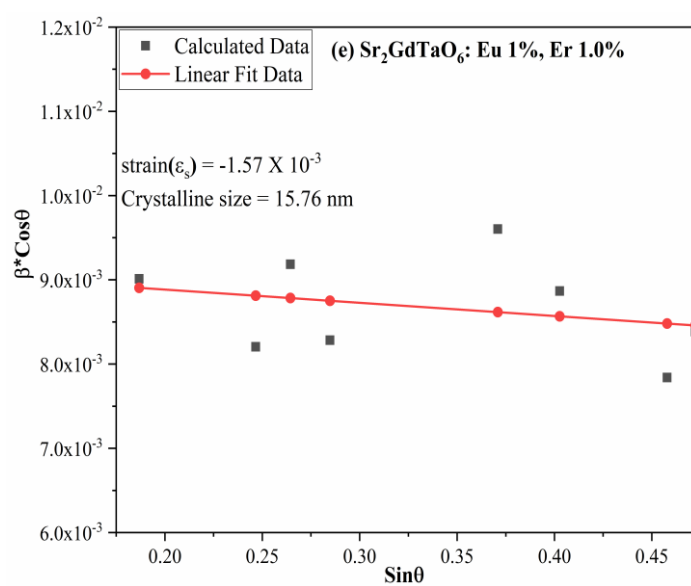
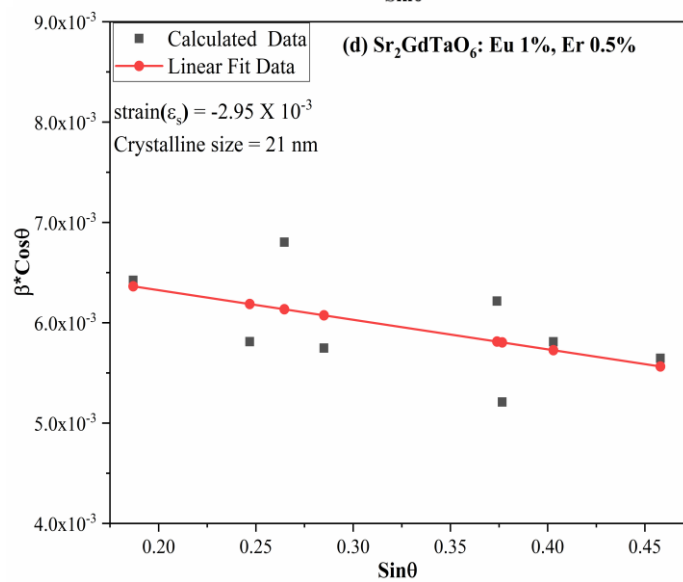
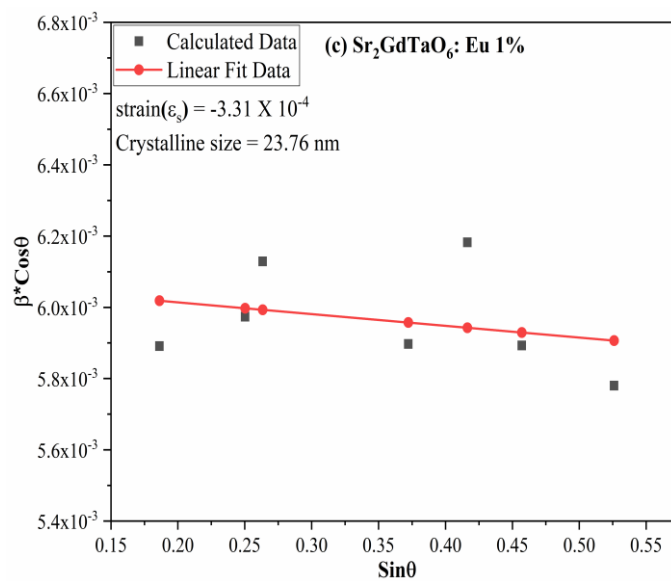
The broadening of XRD peaks reflects the nano crystalline nature of undoped, single doped and Eu(III), Er (III) double doped $\text{Sr}_2\text{GdTaO}_6$ samples. As the effective broadening of XRD peak caused due to lattice strain and small crystallite size, these

two effects can be distinguished. These effects can be calculated by plotting $\beta \cos\theta$ versus $\sin\theta$ as per the following equation (6.3) (Williamson–Hall plot) [33, 40].

$$\beta_{hkl} * \cos\theta_{hkl} = \left(\frac{k\lambda}{D}\right) + \varepsilon * \sin\theta_{hkl} \text{----- (6.3)}$$

The shift in the XRD patterns also reflected in the Williamson–Hall plot, which assigned due to the strained and distorted environment in undoped, single doped, and Eu(III), Er (III) double doped $\text{Sr}_2\text{GdTaO}_6$ phosphors. The crystallite size and strain of all $\text{Sr}_2\text{GdTaO}_6$ are estimated from the intercept and slope of the W-H plot are listed in Table 6.3. The Williamson-Hall plot shows (Figure 6.3 (a-g)), the slope of the line for all samples is negative (compressive) indicates that strain broadening must be very small [41].





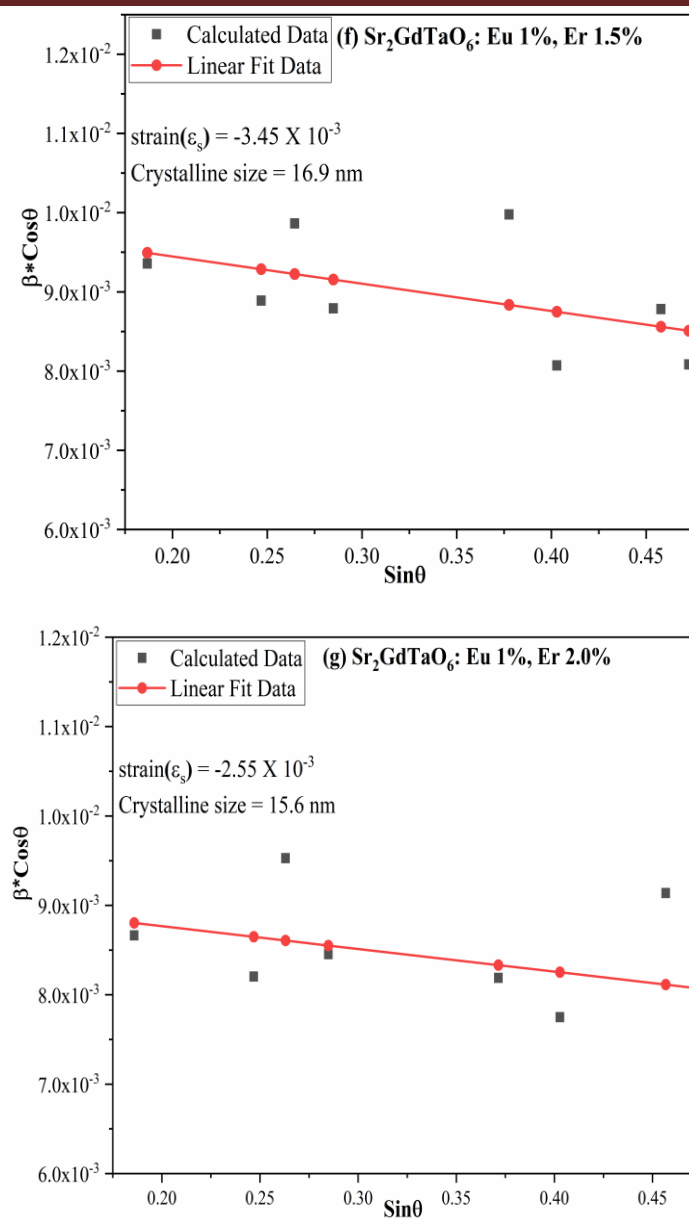


Figure 6.3 (a-g) Williamson–Hall plot of undoped, single doped and Eu(III), Er(III) double doped $\text{Sr}_2\text{GdTaO}_6$.

Sample	$\text{Sr}_2\text{GdTaO}_6$	$\text{Sr}_2\text{GdTaO}_6$: Eu(1%)	$\text{Sr}_2\text{GdTaO}_6$: Er(1%)	$\text{Sr}_2\text{GdTaO}_6$: Eu(1%), Er(0.5%)	$\text{Sr}_2\text{GdTaO}_6$: Eu(1%), Er(1.0%)	$\text{Sr}_2\text{GdTaO}_6$: Eu(1%), Er(1.5%)	$\text{Sr}_2\text{GdTaO}_6$: Eu(1%), Er(2.0%)	
Structure	Monoclinic	Monoclinic	Monoclinic	Monoclinic	Monoclinic	Monoclinic	Monoclinic	
Space Group	$P2_1/n$	$P2_1/n$	$P2_1/n$	$P2_1/n$	$P2_1/n$	$P2_1/n$	$P2_1/n$	
Cell Parameters	a (Å)	6.0156(2)	6.0198(7)	6.0235(6)	6.0189(7)	6.0214(3)	6.0138(1)	6.0125(4)
	b (Å)	6.2589(5)	6.2645(3)	6.2718(4)	6.2573(2)	6.2605(9)	6.2679(6)	6.2725(7)
	c (Å)	8.3089(4)	8.3112(5)	8.3185(1)	8.3125(3)	8.3040(8)	8.3099(5)	8.3025(2)
	β	89.057	89.092	90.012	90.045	90.083	90.018	90.115
Volume (Å) ³	312.84	313.42	314.26	313.06	313.03	313.23	313.11	
Average Crystallite Size (nm)	Scherrer Method	18.12	14.56	24.53	20.88	16.24	16.78	16.2
	W-H Plot	17.83	13.16	23.76	21.15	15.76	16.9	15.6
Strain (ϵ)		-2.77×10^{-3}	-2.47×10^{-3}	-3.31×10^{-3}	-2.95×10^{-3}	-1.57×10^{-3}	-3.47×10^{-3}	-2.55×10^{-3}

Table 6.3 Summary of cell parameter, volume, crystalline size and strain of undoped, single doped and Eu(III), Er(III) double doped $\text{Sr}_2\text{GdTaO}_6$.

6.3.2 FTIR (Fourier Transform Infrared Spectrometry)

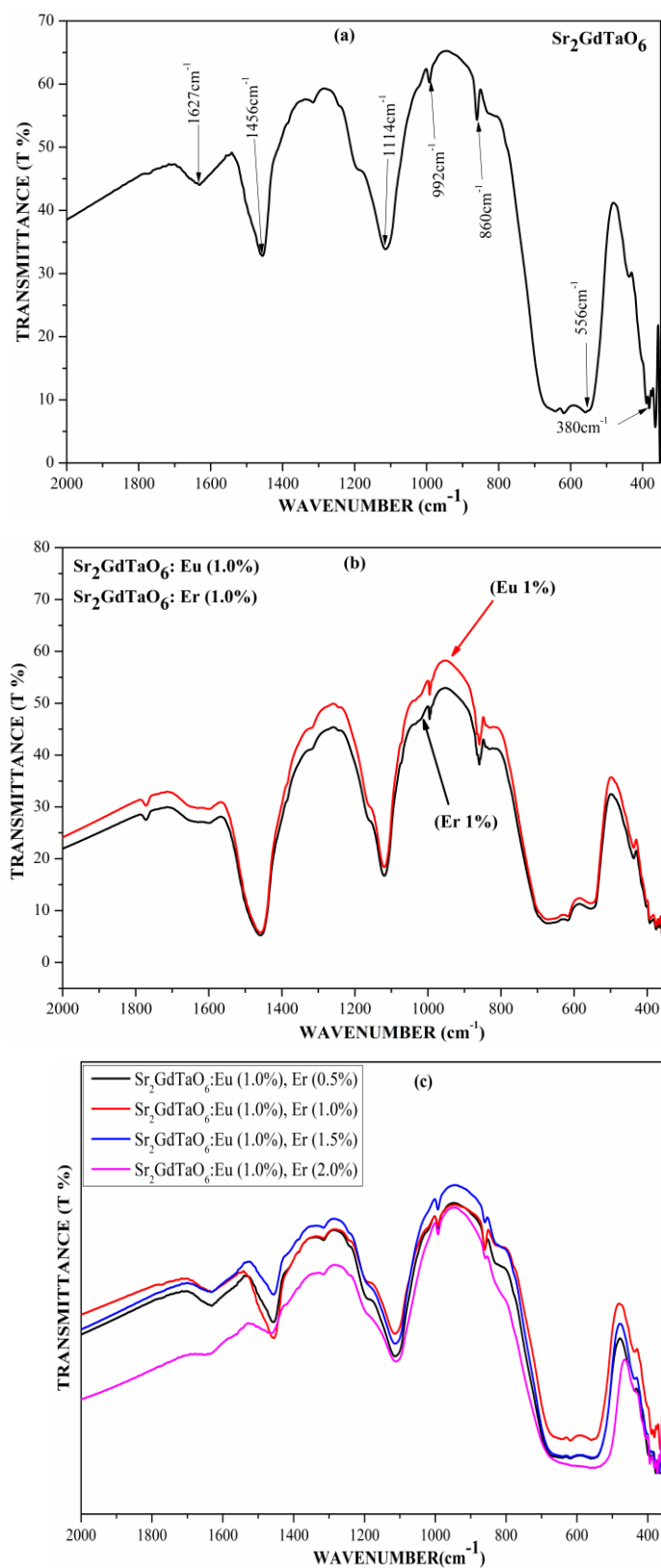


Figure 6.4 FTIR spectra of (a) Undoped $\text{Sr}_2\text{GdTaO}_6$ and (b) single doped $\text{Sr}_2\text{GdTaO}_6$ and (c) Eu(III), Er(III) double doped $\text{Sr}_2\text{GdTaO}_6$.

Figure 6.4 (a-c) exhibits the FTIR transmission pattern of undoped, single doped, and Eu(III), Er (III) double doped $\text{Sr}_2\text{GdTaO}_6$. The FTIR spectra were recorded via the potassium bromide (KBr) pellet structure using the pellet technique. The infrared pattern presents three well-defined bands at 380 cm^{-1} , 566 cm^{-1} , and 1456 cm^{-1} . It's in good cooperation for a perovskite type structure under group theory predictions [41] where the vibrational coupling between the different coordination polyhedral expected. The asymmetric stretching and bending modes of TaO_6 octahedron dominate in the IR spectrum of all $\text{Sr}_2\text{GdTaO}_6$ phosphors. The energy band at 380 cm^{-1} is due to the asymmetric bending of the TaO_6 octahedra while the strong energy band at 566 cm^{-1} attributed to the asymmetric stretching of the TaO_6 octahedra [42]. Perovskite type materials usually present characteristic two band spectra dominated by the antisymmetric F_{10} stretching and deformation modes of the MO_6 octahedra [43–46]. Therefore, in the present case, the strong and broad IR band found at higher energies can be allocated to the antisymmetric stretching to the vibration of the TaO_6 octahedra present in the investigated lattices. The second band, located at around 320 cm^{-1} , is probably of complex origin, involving the mentioned deformational mode of the same octahedra, mixed with modes of the LnO_6 octahedra.

The same spectral pattern, with two strong and well-defined IR bands in the $400\text{--}650\text{ cm}^{-1}$ region, has also been found in a great number of $\text{A}_2\text{BB}'\text{O}_6$ perovskite type materials [47 – 51]. The weak band at around 1456 cm^{-1} likely corresponds to the overtones of the fundamental vibrations in undoped, single doped, and Eu(III), Er (III) double doped $\text{Sr}_2\text{GdTaO}_6$. A very small peak at 1627 cm^{-1} is of the carrier $\text{KBr}\cdot(\text{H}_2\text{O})_n$ [22]. It is to be mentioned that in the present case with the polycrystalline sample and non-polarized light, the other remaining stretching and bending modes are probably too weak to be observed in the transmittance spectrum. The absorption peaks at 992 cm^{-1} and 860 cm^{-1} due to legend formation were assigned to stretching characteristics of SrCO_3 [52].

6.3.3 Photoluminescence

Photoluminescence (PL) is finding more extensive as an experimental window into the electronic structure. PL spectroscopy is a well-recognized method to collect information about the electronic structure, optical and photoelectronic properties of materials, including gap states, shallow and deep defects [53]. PL depends on electronic excitations, and thus it's a significant complement to spectroscopies concerning lattice excitations. In particular, understanding the structures of both fundamental and photo-

excited states is essential for their broad applications and also for their importance in getting insight into the nature of luminescence processes. It allows developing theoretical models for prophesying the nature of the mechanisms for photo-induced processes. Therefore, PL performance driven by controlled filling the development of the electronic structures is one of the most exciting issues of condensed matter physics. The interpretation of the problem opens a possibility to explain the impact of PL behavior and the optical properties of these systems [54].

Synthesis, characterization, and study of luminescence features of perovskite oxides are the subject of several kinds of research. The corresponding electronic structures of perovskite oxides have been analyzed quite broadly by experimental or/and theoretical works [55–65]. These properties revealed important fields of research for such material applications, stimulating further efforts in the study of their response under various conditions.

In the literature, there are several methods to explain the radiative decay taking place in perovskite-like structures. Impurities, surface states, and defects perform an essential role in the PL properties of perovskite-type oxides [56, 66 – 75]. At room temperature, PL is seen in undoped and/ or doped nanocrystalline powders and amorphous thin films of perovskite-type oxides [75 – 85]. Lately, red and green phosphors based on the perovskite structure were analyzed and optimized [86, 87].

The beginning of PL emission can be associated with variation in stoichiometry and the appearance of impurities. From the general phenomenology, the fundamental idea of Landau [88] on intrinsic molecular polarons in ionic solids has a crucial impact on the specific feature of modern research. The approach of self-trapping formerly introduced by Landau explains an excess electron being caught within a potential well in solids. The electron together with the locally distorted lattice around it considered a quasiparticle, which is known as a polaron.

Among the numerous mechanisms for analyzing the origins of PL in perovskite-based materials, the recombination of the self-trapped electron (STEs) [58, 89] and the charge transfer vibronic exciton (CTVE) [90] are the basis of the current proposals to understand the PL behavior. Vikhnin et al. [91, 92], have been proposed the concept of CTVE to explain an exciton structure in perovskite-type materials. The CTVE is a multi-site structure that occurrence induced by charged impurities in ionic-covalent solids [92].

Photoluminescence of Eu (III) doped $\text{Sr}_2\text{GdTaO}_6$

There has been a long-running dispute about the nature of PL appearance in perovskites. Lots of experiments have been performed at room temperature as well as at the low temperature in many perovskites to explain PL behavior [82, 86, 89, 93, 94]. The development of room-temperature PL emission in amorphous type perovskite encourages notable research interests for room temperature PL of perovskite materials.

Now it's well known that optical properties like PL depend on both structural and electronic properties with compositional regulation, and the appearance of impurities and defects. In addition, there is a piece of experimental confirmation has been exhibited that room temperature PL can't be seen in well-crystallized perovskite phosphors [83, 95–98]. The PL is a quantum phenomenon, and for luminescence to appear there should be specific mid-gap states in the forbidden band.

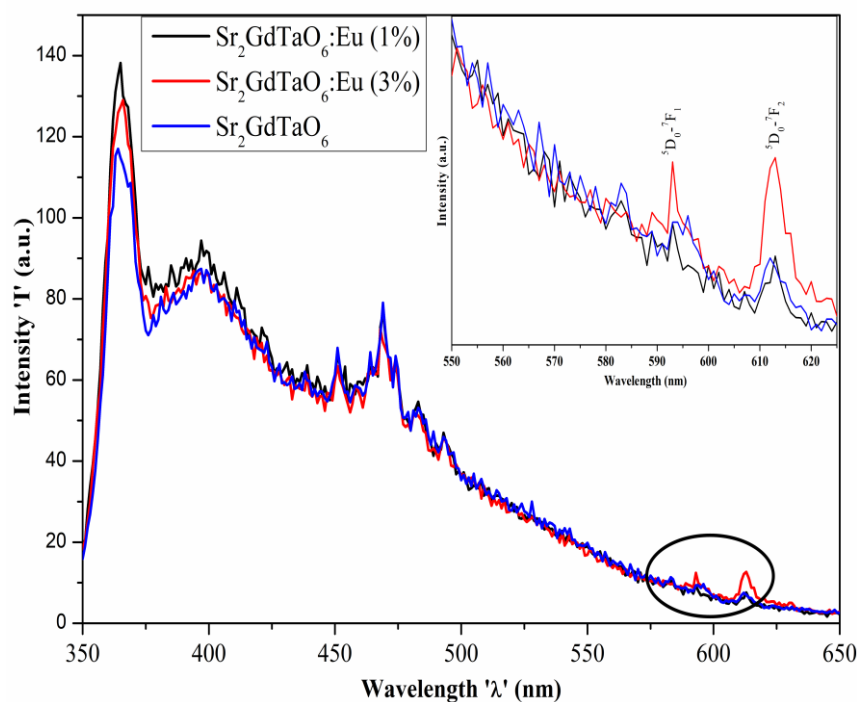


Figure 6.5 PL spectra of $\text{Sr}_2\text{GdTaO}_6$, $\text{Sr}_2\text{GdTaO}_6:\text{Eu}$ (1%) and $\text{Sr}_2\text{GdTaO}_6:\text{Eu}$ (3%).

Figure 6.5 exhibits photoluminescence spectra of undoped and Eu(III) doped $\text{Sr}_2\text{GdTaO}_6$. A magnified portion from 575 nm to 625 nm of PL of undoped and 1% and 3% Eu^{3+} doped $\text{Sr}_2\text{GdTaO}_6$ displayed in inset figure. In the magnified portion, there is a small effect of Eu^{3+} in the PL spectra of $\text{Sr}_2\text{GdTaO}_6$. Limited number of PL emission of Eu^{3+} maybe due to crystal field quenching effect observed in emission spectra of $\text{Sr}_2\text{GdTaO}_6$.

Production of visible luminescence in rare-earth ion-doped materials as a result of continuous photon absorption in excited levels was introduced in 1959 and has been termed as “quantum counter action” [99]. Now, the same effect usually called excited-state absorption (ESA) in contrast with ground-state absorption (GSA). This effect is observed particularly at high excitation densities such as produced by high-power laser light excitation or encountered in single-mode optical fibers.

Photoluminescence of Eu (III), Er (III) double doped $\text{Sr}_2\text{GdTaO}_6$

Luminescence spectra of Eu (III) compounds are more informative than the identical absorption spectra. Eu (III) containing many compounds show strong photoluminescence due to the $^5\text{D}_0 \rightarrow ^7\text{F}_J$ transitions ($J = 0 - 6$) from the $^5\text{D}_0$ excited state to the J levels of the ^7F ground state. Ordinarily, the transitions from $^5\text{D}_0$ to $^7\text{F}_5$ and $^7\text{F}_6$ levels are not observed as they are outside the wavelength range of the detectors of spectrofluorimeter. The conclusion made from the analysis of different positions of $^5\text{D}_0 \rightarrow ^7\text{F}_J$ transitions is the distance between J and J + 1 line, which is increases with increasing the J value. The $^5\text{D}_0 \rightarrow ^7\text{F}_1$ transition is very close to the $^5\text{D}_0 \rightarrow ^7\text{F}_0$ transition, but $^5\text{D}_0 \rightarrow ^7\text{F}_6$ transition is prevailing more than 50 nm further to the infrared than the $^5\text{D}_0 \rightarrow ^7\text{F}_5$ transition [100].

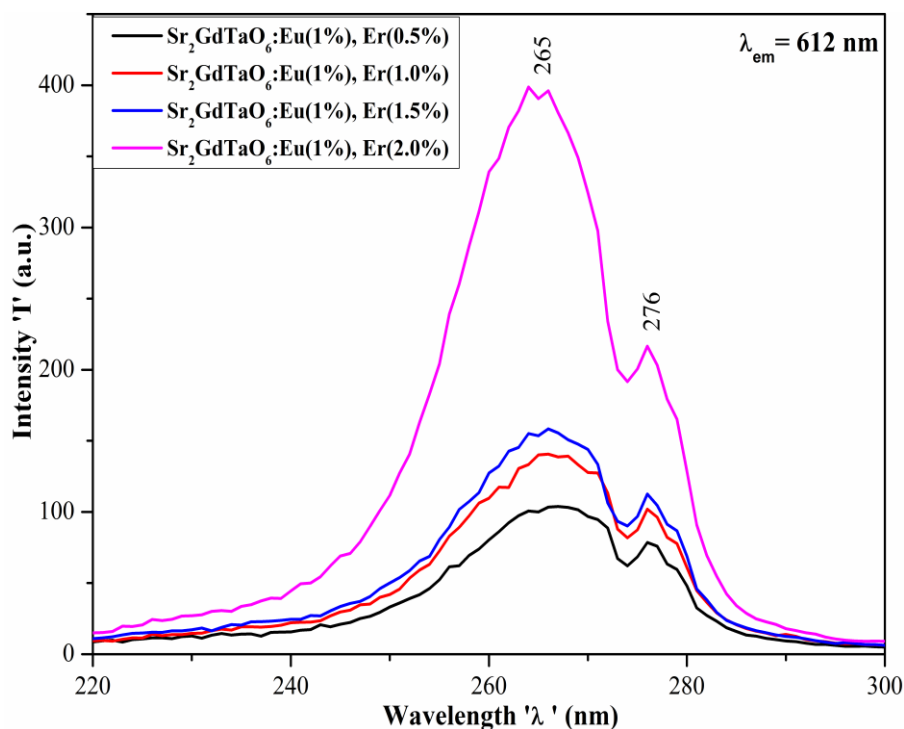


Figure 6.6 Photoluminescence excitation spectra of Eu(III), Er(III) double doped $\text{Sr}_2\text{GdTaO}_6$.

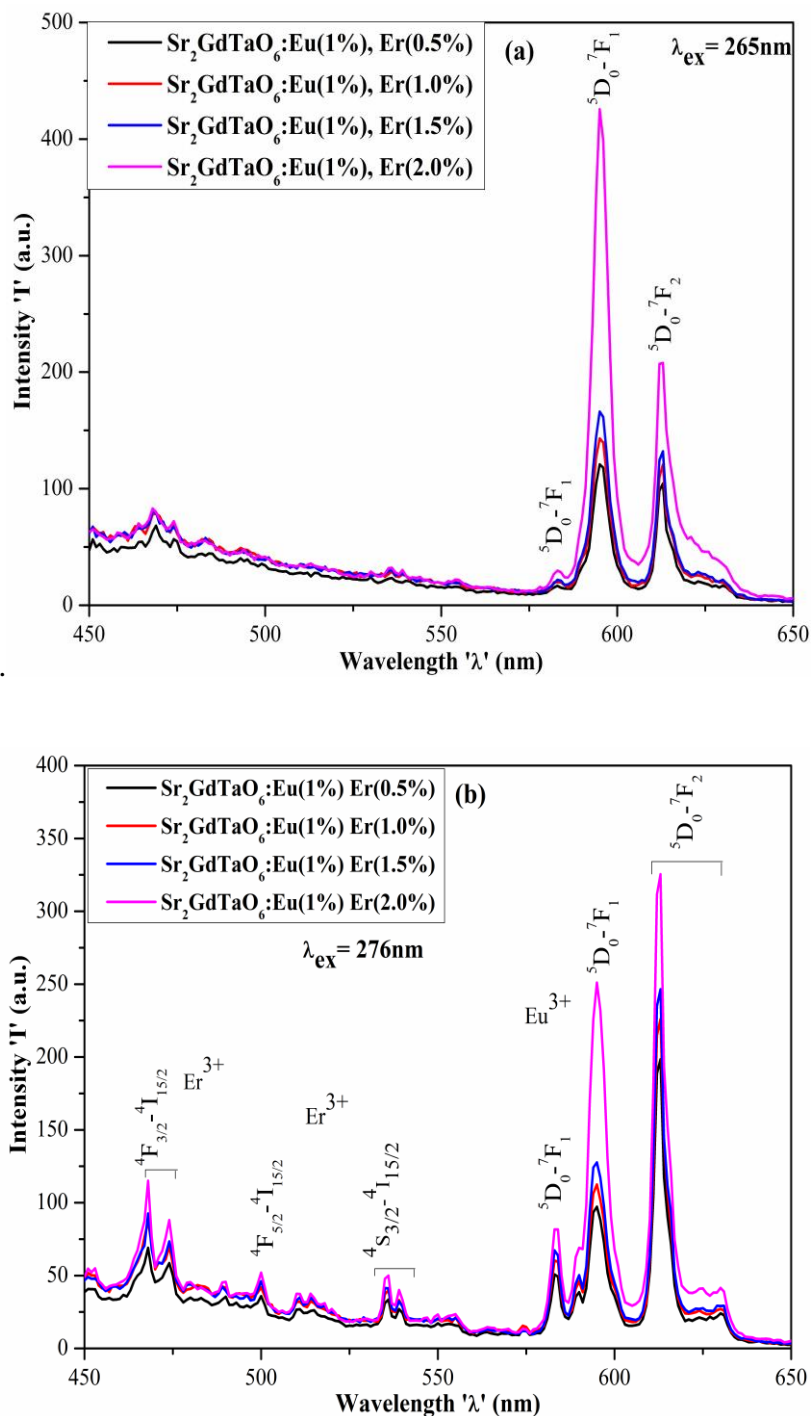


Figure 6.7 Photoluminescence spectra of Eu(III), Er(III) double doped $\text{Sr}_2\text{GdTaO}_6$ of excitation wavelength (a) 265nm and (b) 276nm.

This function can be described by the fact that the splitting of the ${}^7\text{F}_J$ multiplet corresponds quite well to the Landé interval rule. The Landé interval rule is an interval between consecutive energy levels is proportional to the larger of their total angular momentum values J (i.e., the splitting increases with increasing J values). The majority of transitions in the luminescence spectrum are due to electric dipole transitions. An

electric dipole transition is an outcome of the interaction of lanthanide ion with the electric field vector within an electric dipole. The linear movement of charges is considered the origin of an electric dipole. The electric dipole operator has odd transformation features strengthening inversion towards an inversion center. Intraconfigurational electric dipole transitions (e.g., s-s, p-p, d-d, or f-f transitions) are bordered by the Laporte selection rule. This rule rigidly refers to lanthanide ion in a centrosymmetric environment. But this rule is relaxed for lanthanide ions implanted in a medium. As this transition is partly allowed by vibronic coupling or by combining higher configurations into 4f wave functions by the crystal-field effect, these transitions are much weaker compared to ordinary electric dipole transitions. These transitions are called induced electric dipole transitions or forced electric dipole transitions. The intensities of the electric dipole transitions can be described by the Judd–Ofelt theory [107–112].

Some transitions such as the ${}^5D_0 \rightarrow {}^7F_1$ transition have magnetic dipole character. Magnetic dipole transitions (MD transitions) are allowed by the Laporte selection rule, but their intensities are weak and comparable to those of the induced electric dipole transitions [106]. The intensity of a magnetic dipole transition is mostly independent of the environment, and it can be considered in a first approach to be constant. A magnetic dipole transition is induced by the interaction of the lanthanide ion with the magnetic field component of the light by a magnetic dipole. If a charge removed over a curved path through the transition, the transition will own a magnetic dipole character. The curve of the displacement will be weakly visible in a volume as small as the extent of a lanthanide ion, so that magnetic dipole transitions have low intensity. Magnetic dipole emission also can be considered as a rotational displacement of charge. Since the function of rotation not changed under inversion by an inversion center, a magnetic dipole transition has even parity. Therefore, magnetic dipole operator occupies even transformation properties under inversion and allows transitions between states with even parity (i.e., intra-configurational transitions such as 4f–4f transitions) [113–115].

Figure 6.6 shows room-temperature photoluminescence excitation spectra at 616nm. This PLE spectrum shows broad band with peak at 265nm and 276nm from the intra configuration of the 4f–4f transitions of Eu^{3+} . The broad band peaking at 265 nm can be ascribed to the charge transfer (CT) transition of the filled 2p orbitals of O^{2-} ions to the partially filled 4f orbitals of Eu^{3+} ions when in the octahedral field, of which the position is mainly determined by the Eu – O distance [116]. When smaller Eu^{3+} ions

substitute the Sr^{2+} sites, the lattice shrinks and the Eu – O bond becomes shorter and stronger, which will take more energy to break, thus a blue shift of CT band emerge [117, 118]. Figure 6.7 (a & b) displays typical emission spectra of radiation emanating from the Eu(III), Er (III) double doped $\text{Sr}_2\text{GdTaO}_6$ phosphors excited at 265nm and 276nm with a fixed europium concentration of 1.0mol% and increasing erbium concentration from 0.5 to 2.0mol% with an increment of 0.5 mol%. These phosphors were excited using xenon lamp operated at a 265nm and 276nm. The Eu(III), Er (III) double doped $\text{Sr}_2\text{GdTaO}_6$ samples exhibited two visible emission peaks around 596 and 614 nm, which were assigned to the magnetic and electric dipole transitions ($^5\text{D}_0 \rightarrow ^7\text{F}_1$, $^5\text{D}_0 \rightarrow ^7\text{F}_2$) of europium when excited at 265nm. While Eu(III), Er (III) double doped $\text{Sr}_2\text{GdTaO}_6$ exhibited five distinct visible emission bands around 468nm, 474nm, 584nm, 596nm, and 614nm. These are assigned to the electric transition ($^4\text{F}_{3/2} \rightarrow ^4\text{I}_{15/2}$) of erbium and magnetic and electric dipole transitions ($^5\text{D}_0 \rightarrow ^7\text{F}_1$, $^5\text{D}_0 \rightarrow ^7\text{F}_2$) of europium when excited at 276nm, respectively.

Emission peaks with low-intensity at 499nm, 535nm, and 538nm were seen and assigned to the electric transition of $^4\text{F}_{5/2} \rightarrow ^4\text{I}_{15/2}$ and $^4\text{S}_{3/2} \rightarrow ^4\text{I}_{15/2}$ of erbium [119, 120]. The emission peaks at 584nm, 596nm, and 614nm are associated with energy transitions from high energy levels $^5\text{D}_1$ and $^5\text{D}_0$ to low energy levels of $^7\text{F}_J$ ($J=0-6$) [121]. From Figure 6.7, an intense emission peak at 614 nm can be ascribed to the hypersensitive electric dipole transition of the $^5\text{D}_0 \rightarrow ^7\text{F}_2$. The emission peaks with the range of 580–600 nm are due to the magnetic dipole transition ($^5\text{D}_0 \rightarrow ^7\text{F}_1$) of europium has a lower intensity than the $^5\text{D}_0 \rightarrow ^7\text{F}_2$ transition when it excited at 276nm, revealing that Eu^{3+} ions are at the non-inversion symmetric positions [122, 123]. The emission peaks in the range of 610-630 nm are due to the electric dipole transition of $^5\text{D}_0 \rightarrow ^7\text{F}_2$ has a lower intensity than the $^5\text{D}_0 \rightarrow ^7\text{F}_1$ transition at excited with 265nm [124].

It is important to note that both emission spectra show a peak at 614nm in the red region, which is attributed to the $^5\text{D}_0 \rightarrow ^7\text{F}_2$ transition. Red emission due to the Eu^{3+} luminescence center has a better perception of the human eye. This red emission is attributed to the electric dipole transition ($^5\text{D}_0 \rightarrow ^7\text{F}_2$) of Eu^{3+} , which is forbidden electric dipole transition. However, an admixture of odd-parity electronic configuration to pure 4f orbitals (like a non-centrosymmetric crystal field component) [125, 126] can partially allow the electric dipole transitions, and their expectation is much higher than the probability of parity-allowed magnet dipole transition ($^5\text{D}_0 \rightarrow ^7\text{F}_2$) [109]. The site

symmetry of Eu^{3+} ion in the host lattice can be predicted by asymmetry ratio which can be defined as equation (6.4),

$$\text{Asymmetry - ratio} = \frac{I(^5D_0 \rightarrow ^7F_2)}{I(^5D_0 \rightarrow ^7F_1)} \text{-----} \quad (6.4)$$

Where, $I(^5D_0 \rightarrow ^7F_2)$ and $I(^5D_0 \rightarrow ^7F_1)$ are the intensities of electric dipole and magnet dipole transitions respectively. For asymmetry ratio >1 , Eu^{3+} substituted at the non-centrosymmetric site while for asymmetry ratio <1 , Eu^{3+} substituted at a centrosymmetric site in the host lattice. In present work, the asymmetric ratio is greater than unity (1) for phosphors excited at 276nm, which intimates that Eu^{3+} is displaced at A site in host lattice, and it's in good agreement with earlier reports [127–131]. Table-6.4 shows the asymmetry ratio for both the emission spectra. Here it's noted that the substitution of Eu^{3+} at Sr^{2+} site in $\text{Sr}_2\text{GdTaO}_6$ is followed by Sr^{2+} ion vacancy (due to charge imbalance) and lattice strain (due to different ionic radius). These defects in lattice lower the local site symmetry of the Eu^{3+} ion and also act as a luminescence quenching center.

Figure 6.8 displays an energy level diagram of Eu(III) and Er(III) ion to explain PLE and PL mechanisms. With 265nm and 276nm excitation wavelength, electrons jump from the ground state to the excited state. After that, electrons are relaxed to the lowest level 5D_0 by using non-radiative transition (NR). In the end, luminescence occurs through the radiative transition $^5D_0 - ^7F_j$ ($j = 0, 1, 2$). Hence, the luminescence emission process is composed of several transitions [132 - 134].

The outcomes from Figure 6.7 (a & b) reveals that the spectral profile of phosphors show remarkable variations with raising erbium concentration concerning the mixed emission light chromaticity when more green light element added to the overall mixed emission fluorescence.

Sr. No.	Sample	Asymmetry Ratio	
		at 265nm	at 276nm
1	$\text{Sr}_2\text{GdTaO}_6$: Eu(1%), Er(0.5%)	0.86	2.04
2	$\text{Sr}_2\text{GdTaO}_6$: Eu(1%), Er(1.0%)	0.84	2.00
3	$\text{Sr}_2\text{GdTaO}_6$: Eu(1%), Er(1.5%)	0.79	1.93
4	$\text{Sr}_2\text{GdTaO}_6$: Eu(1%), Er(2.0%)	0.48	1.295

Table 6.4 Asymmetric ratio of Eu(III) , Er(III) double doped $\text{Sr}_2\text{GdTaO}_6$ for excitation wavelength of 265nm and 276nm emission spectra.

Down conversion mechanism

Luminescence generated in phosphor materials is due to the presence of activator ion. Through external energy excitation, the host lattice absorbs the energy and transfers it to the activator ion. The doped ion experiences excitation from ground level to higher energy levels. After that, it gets relaxed and then radiates a photon of lesser energy that seems like a peak in photoluminescence emission spectra. Eu^{3+} has $4f_6$ configuration where europium possesses (${}^7F_{0-6}$) ground states and (${}^5D_{0-3}$) excited states. Figure 6.7 depicts the transitions of Eu^{3+} ion in the undertaken host material [135].

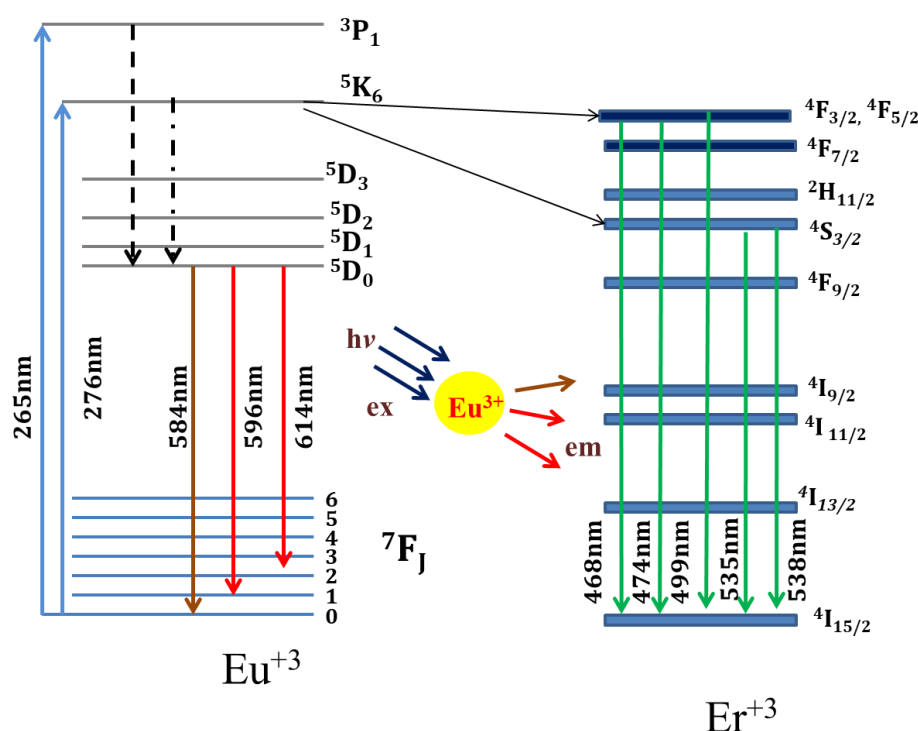


Figure 6.8 Energy level diagram of Eu(III), Er(III) double doped $\text{Sr}_2\text{GdTaO}_6$.

The down conversion emission spectra of Eu(III), Er(III) double doped $\text{Sr}_2\text{GdTaO}_6$ phosphor shown in Figure 6.7 (a & b). The fluorescence spectrum display high-intensity peaks at 596 nm and 614 nm excited at 265 nm and 276nm, appearing due to ${}^5D_0 \rightarrow {}^7F_1$ and ${}^5D_0 \rightarrow {}^7F_2$ transitions of Eu^{3+} ions. The magnetic dipole and electric dipole transitions of Eu^{3+} ($\Delta J = 0, \pm 1, \pm 2$) are hypersensitive to site symmetry, and the effect seen with very intense ${}^5D_0 \rightarrow {}^7F_1$ and ${}^5D_0 \rightarrow {}^7F_2$ transitions. It has indicated that under UV excitation, the same phosphor shows orange color emission, which confirms the down-conversion of the UV wavelength to the visible wavelength.

Figure 6.6 shows the photoluminescence excitation (PLE) spectra of Eu(III), Er(III) double doped $\text{Sr}_2\text{GdTaO}_6$ phosphor at 614 nm. The PLE spectrum shows broadband from 245 to 285 nm due to the charge transfer absorption of the $(\text{TaO}_6)^{7-}$ in the host $\text{Sr}_2\text{GdTaO}_6$ phosphor and sensitizing the activator Eu^{3+} ion [136]. The broadband in PLE clearly shows the efficient charge transfer process between the hosts ($\text{Sr}_2\text{GdTaO}_6$) to the activator (Eu^{3+}).

CIE (Commission International del'éclairage)

The emission spectra were examined and the chromaticity color coordinates of all samples were calculated and are presented in the Commission International del'éclairage (CIE) 1931 diagram in Figure 6.9 (a-b). With the increasing erbium concentration, the color tone of the emanating light shifts from orange to the red region. The results also show that the Eu(III), Er(III) double-doped phosphors herein reported extended further to the latitude of the orange-red tenability region after compared to reported results [137 – 139]. Moreover, it's good to point out that the combination of the emission color corresponding to coordinate points (Figure 6.9 (a-b)) yields a mixture of light with color in the white-light region possess glow correlated color temperature, i.e., CCT in the 3000K – 6000K range. We have admittedly simulated the generation flow CCT for white-light using xenon lamp and the phosphors herein reported [140 – 142]. Table-6.5 shows the CIE1931 coordinates and associated correlated color temperature of the overall emission. One can see that the white-light generated exhibits low CCT owing to the presence of red components in the emission spectra of the Eu(III), Er(III) double-doped phosphors.

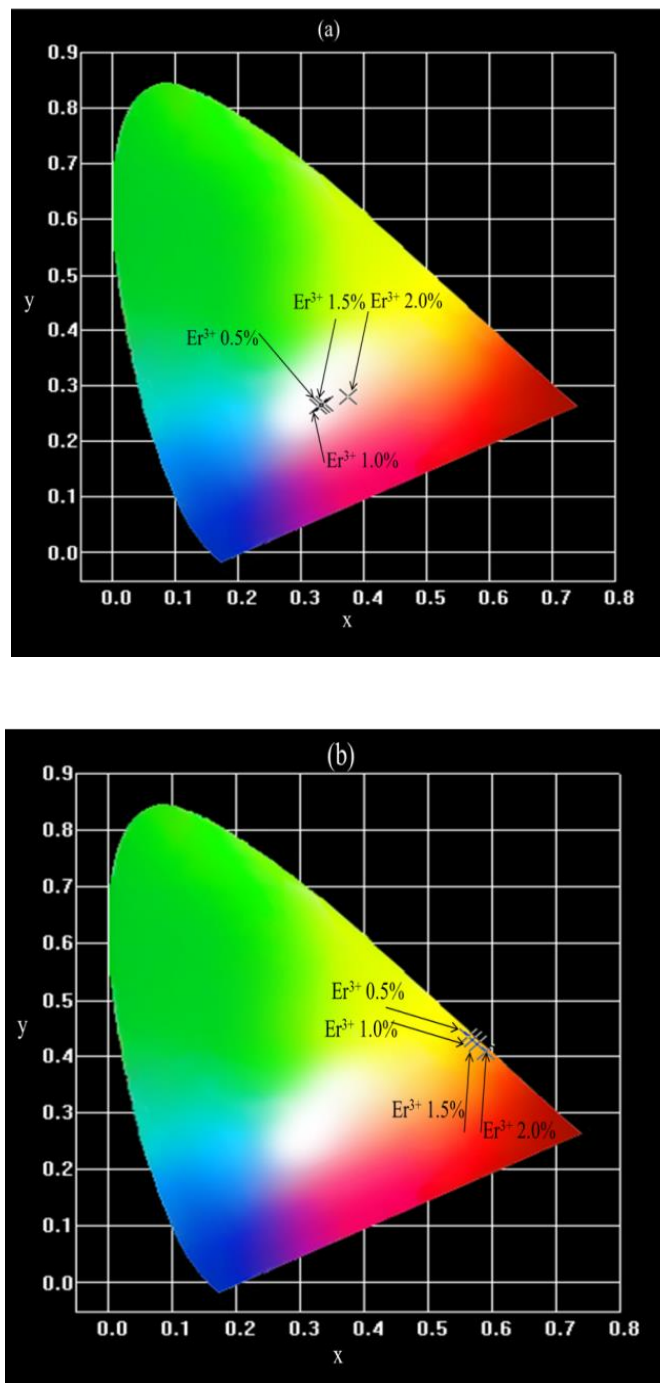


Figure 6.9 CIE diagram of phosphor excited at (a) 265nm and (b) 276nm for fixed Eu^{3+} content of 1.0mol% and Er^{3+} : (1) 0.5mol%; (2) 1.0 mol%; (3) 1.5 mol%; (4) 2.0 mol%.

Sr. No.	Sample	265nm				276nm			
		x	y	CCT		x	y	CCT	
				Calcu.	Software			Calcu.	Software
1	Sr ₂ GdTaO ₆ : Eu(1%), Er(0.5%)	0.563	0.435	1842	1852	0.333	0.266	5370	5388
2	Sr ₂ GdTaO ₆ : Eu(1%), Er(1.0%)	0.569	0.431	1783	1790	0.328	0.262	5850	5874
3	Sr ₂ GdTaO ₆ : Eu(1%), Er(1.5%)	0.578	0.423	1680	1692	0.337	0.268	5030	5048
4	Sr ₂ GdTaO ₆ : Eu(1%), Er(2.0%)	0.577	0.418	1668	1675	0.374	0.279	3129	3075

Table 6.5 CIE 1931 coordinates and correlated color temperature of the emissions under (265nm and 276nm) xenon lamp excitation of Eu(III), Er(III) double doped Sr₂GdTaO₆ phosphor.

6.4 Outcome

Undoped, single doped and double doped Strontium Gadolinium Tantalum (SGT) oxide has been synthesized by the combustion synthesis method. The X-ray diffraction measurement of all Strontium Gadolinium Tantalum (SGT) oxide phosphors reveals that phosphors have a monoclinic phase with $P2_1/n$ (# 014) space group. Prepared perovskite phosphors are nanocrystalline in size measured through Scherrer's method and Williamson-hall plot method. Angle Shift in XRD patterns is also reflected in the Williamson–Hall plot, which occurred due to the highly strained and distorted environment in the Sr_2GdTaO_6 lattice.

FTIR spectra of Sr_2GdTaO_6 gives information that phosphor has a nano-size perovskite structure with an edge-connected Ta-O octahedral. The energy band at 380 cm^{-1} is due to the asymmetric bending of the TaO_6 octahedra. The strong energy band at 566 cm^{-1} attributed to the asymmetric stretching of the TaO_6 octahedra. The weak band at around 1456 cm^{-1} likely corresponds to the overtones of the fundamental vibrations in undoped, single doped, and Eu(III), Er (III) double doped Sr_2GdTaO_6 . A very small peak at 1627 cm^{-1} is of the carrier $KBr.(H_2O)_n$. The absorption peaks at 992 cm^{-1} and 860 cm^{-1} due to legend formation were assigned to stretching characteristics of $SrCO_3$.

Room temperature photoluminescence spectra of phosphor recorded using a Xenon lamp as a source. There is a very small effect of Eu^{3+} in the PL spectra of Sr_2GdTaO_6 , this happens maybe due to crystal field quenching.

PLE spectrum for Eu^{3+} and Er^{3+} doped Sr_2GdTaO_6 shows broad band with peak at 265nm and 276nm from the intra configuration of the 4f–4f transitions of Eu^{3+} . The broad band peaking at 265 nm can be ascribed to the charge transfer (CT) transition of the filled 2p orbitals of O^{2-} ions to the partially filled 4f orbitals of Eu^{3+} ions when in the octahedral field, of which the position is mainly determined by the Eu – O distance. Emission spectra shows emission peaks at 584nm, 596nm, and 614nm of Eu^{3+} . Emission peaks with low-intensity at 499nm, 535nm, and 538nm were seen and assigned to the electric transition of ${}^4F_{5/2} \rightarrow {}^4I_{15/2}$ and ${}^4S_{3/2} \rightarrow {}^4I_{15/2}$ of erbium. The spectral profile of phosphors shows remarkable variations with raising erbium concentration concerning the mixed emission light chromaticity when more green light element added to the overall mixed emission fluorescence. The emission color corresponding to coordinate points yields a mixture of light with color in the white-light region possess glow correlated color temperature, i.e., CCT in the 3000K – 6000K

range. The white-light generated exhibits low CCT owing to the presence of red components in the emission spectra of the Eu(III), Er(III) double-doped phosphors. Eu(III), Er(III) double-doped phosphor propose for tunable solid state lightning.

References

- [1] T. E. Warner, *Synthesis, Properties and Mineralogy of Important Inorganic Materials*. Chichester, UK: John Wiley & Sons, Ltd, 2011.
- [2] H. Asano, J. Hayakawa, and M. Matsui, "Preparation and properties of triple perovskite $\text{La}_{3-3x}\text{Ca}_{1+3x}\text{Mn}_3\text{O}_{10}$ ferromagnetic thin films," *Appl. Phys. Lett.*, vol. 71, no. 6, pp. 844–846, Aug. 1997.
- [3] A. P. Mackenzie *et al.*, "Quantum Oscillations in the Layered Perovskite Superconductor Sr_2RuO_4 ," 1996.
- [4] W. J. Merz, "Switching Time in Ferroelectric BaTiO_3 and Its Dependence on Crystal Thickness," *J. Appl. Phys.*, vol. 27, no. 8, pp. 938–943, Aug. 1956.
- [5] Y. Maeno *et al.*, "Superconductivity in a layered perovskite without copper," *Nature*, vol. 372, no. 6506, pp. 532–534, Dec. 1994.
- [6] J. Torrance, P. Lacorre, A. Nazzari, E. Ansaldo, and C. Niedermayer, "Systematic study of insulator-metal transitions in perovskites RNiO_3 (R=Pr,Nd,Sm,Eu) due to closing of charge-transfer gap," *Phys. Rev. B*, vol. 45, no. 14, pp. 8209–8212, Apr. 1992.
- [7] C. Bohnke and J. L. Fourquet, "Mechanism of ionic conduction and electrochemical intercalation of lithium into the perovskite lanthanum lithium titanate," *Solid State Ionics*, vol. 91, no. 1–2, pp. 21–31, 1996.
- [8] A. Sani, M. Hanfland, and D. Levy, "Pressure and Temperature Dependence of the Ferroelectric ^ Paraelectric Phase Transition in PbTiO_3 ," *J. Solid State Chem.*, vol. 452, no. 2, pp. 446–452, 2002.
- [9] W. Rainer, B. Tudor, and H. Karl-Heinz, "dc Electrical Degradation of Perovskite-Type Titanates: I, Ceramics," *J. Am. Ceram. Soc.*, vol. 73, no. 6, pp. 1645–1653, 1990.
- [10] R. M. Wentzcovitch, B. B. Karki, S. Karato, and C. R. S. Da Silva, "High pressure elastic anisotropy of MgSiO_3 perovskite and geophysical implications," *Earth Planet. Sci. Lett.*, vol. 164, no. 1–2, pp. 371–378, 1998.

- [11] N. Alexandra and W. Donald J., *Pervoskite: A Structure of Great Interest to Geophysics and Materials Science*. Washington, D. C.: American Geophysical Union, 1989.
- [12] M. Osako and I. Eiji, "THERMAL DIFFUSIVITY OF MgSiO₃ PEROVSKIT," *Geophys. Reach. Lett.*, vol. 18, no. 2, pp. 239–242, 1991.
- [13] H. Piel, "HIGH T_c SUPERCONDUCTORS FOR ACCELERATOR CAVITIES," *Nucl. Instruments Methods Phys. Res. Sect. A Accel. Spectrometers, Detect. Assoc. Equip.*, vol. 4287, no. 1–2, pp. 294–305, 1990.
- [14] S. Nagata *et al.*, "Recent research activities on functional ceramics for insulator, breeder and optical sensing systems in fusion reactors," *J. Nucl. Mater.*, vol. 442, no. 1–3, pp. S501–S507, 2013.
- [15] A. K. De, B. Luckscheiter, W. Lutze, G. Malow, and E. Schiewer, "Development of glass ceramics for the incorporation of fission products," *Am. Ceram. Soc. Bull.*, vol. 55, no. 5, pp. 500–503, 1976.
- [16] J. Zhu *et al.*, "Pervoskite Oxides: Preparation, Characterizations, and Applications in Heterogeneous Catalysis," *ACS Catal.*, vol. 4, no. 9, pp. 2917–2940, 2014.
- [17] B. Seyfi, M. Baghalha, and H. Kazemian, "Modified LaCoO₃ nano-pervoskite catalysts for the environmental application of automotive CO oxidation," vol. 148, no. 2–3, pp. 306–311, 2009.
- [18] Y. Liu *et al.*, "BaSrTiO₃ Interdigitated Capacitors for Distributed Phase Shifter Applications," *IEEE Microw. Guid. Wave Lett.*, vol. 10, no. 11, pp. 448–450, 2000.
- [19] B. Xu *et al.*, "Room-temperature ferromagnetism and ferroelectricity in Fe-doped BaTiO₃," *Phys. Chem. Chem. Phys.*, vol. 79, pp. 2–6, 2009.
- [20] J. Kreisel, A. M. Glazer, G. Jones, P. A. Thomas, L. Abello, and G. Lucazeau, "An x-ray diffraction and Raman spectroscopy investigation of A-site substituted pervoskite compounds: the (Na_{1-x}K_x)_{0.5}Bi_{0.5}TiO₃ (0 ≤ x ≤ 1) solid solution," *J. Phys. Condens. Matter*, vol. 12, no. 14, pp. 3267–3280, Apr. 2000.
- [21] I. V Solovyev, "Electronic structure and stability of the ferrimagnetic ordering in double pervoskites," *Phys. Rev. B - Condens. Matter Mater. Phys.*, vol. 65, pp. 1–17, 2002.
- [22] B. Ghosh, A. Dutta, and T. P. Sinha, "Vibrational modes and electrical transport

- in Sr₂GdTaO₆,” *Mater. Chem. Phys.*, vol. 143, no. 1, pp. 26–33, Dec. 2013.
- [23] M. Srinivas, V. Verma, N. Patel, D. Modi, D. Tawde, and K. V. R. Murthy, “Characterization of newly synthesized Strontium Cerium Niobate nanophosphor,” *J. Lumin.*, vol. 147, pp. 324–327, Mar. 2014.
- [24] L. A. Khalam and M. T. Sebastian, “Effect of Cation Substitution and Non-Stoichiometry on the Microwave Dielectric Properties of Sr(B’_{0.5}Ta_{0.5})O₃ [B’=Lanthanides] Pervoskites,” *J. Am. Ceram. Soc.*, vol. 89, no. 12, pp. 3689–3695, Dec. 2006.
- [25] H. Zhang, X. Fu, S. Niu, and Q. Xin, “Synthesis and photoluminescence properties of Eu³⁺-doped AZrO₃ (A=Ca, Sr, Ba) pervoskite,” *J. Alloys Compd.*, vol. 459, no. 1–2, pp. 103–106, Jul. 2008.
- [26] D. Sun, D. Li, Z. Zhu, J. Xiao, Z. Tao, and W. Liu, “Photoluminescence properties of europium and titanium co-doped BaZrO₃ phosphors powders synthesized by the solid-state reaction method,” *Opt. Mater. (Amst.)*, vol. 34, no. 11, pp. 1890–1896, 2012.
- [27] Y. Pan *et al.*, “Synthesis and red luminescence of Pr³⁺-doped CaTiO₃ nanophosphor from polymer precursor,” *J. Solid State Chem.*, vol. 174, no. 1, pp. 69–73, Aug. 2003.
- [28] Z. Lu, L. Chen, Y. Tang, and Y. Li, “Preparation and luminescence properties of Eu³⁺-doped MSnO₃ (M = Ca, Sr and Ba) pervoskite materials,” *J. Alloys Compd.*, vol. 387, no. 1–2, pp. L1–L4, Jan. 2005.
- [29] Y. Wang, Y. Sun, J. Zhang, Z. Ci, Z. Zhang, and L. Wang, “New red Y_{0.85}Bi_{0.1}Eu_{0.05}V_{1-y}MyO₄ (M=Nb, P) phosphors for light-emitting diodes,” *Phys. B Condens. Matter*, vol. 403, no. 12, pp. 2071–2075, Jun. 2008.
- [30] S. Neeraj, N. Kijima, and A. . Cheetham, “Novel red phosphors for solid-state lighting: the system NaM(WO₄)_{2-x}(MoO₄)_x:Eu³⁺ (M=Gd, Y, Bi),” *Chem. Phys. Lett.*, vol. 387, no. 1–3, pp. 2–6, Mar. 2004.
- [31] Y. Yuan, X. Zhang, L. Liu, X. Jiang, and J. Lv, “Synthesis and photocatalytic characterization of a new photocatalyst BaZrO₃,” *Int. J. Hydrogen Energy*, vol. 33, no. 21, pp. 5941–5946, 2008.
- [32] R. Borja-urby, L. A. Diaz-torres, P. Salas, M. Vega-gonzalez, and C. Angeles-chavez, “Blue and red emission in wide band gap BaZrO₃:Yb³⁺,Tm³⁺,” *Mater. Sci. Eng.*, vol. 174, no. 1–3, pp. 169–173, 2010.

- [33] C. Suryanarayana and M. G. Norton, *X-Ray Diffraction*, 1st ed. Boston, MA: Springer US, 1998.
- [34] R. D. Shannon, "Revised effective ionic radii and systematic studies of interatomic distances in halides and chalcogenides," *Acta Crystallogr. Sect. A*, vol. 32, no. 5, pp. 751–767, Sep. 1976.
- [35] M. W. Lufaso and P. M. Woodward, "Prediction of the crystal structures of perovskites using the software program SPuDS," *Acta Crystallogr. Sect. B*, vol. 57, no. 6, pp. 725–738, 2001.
- [36] E. Climent-pascual, R. Ruiz-bustos, and R. Sa, "Non-collinear magnetic structure of the Sr₂ErRuO₆ double perovskite," *Prog. Solid State Chem.*, vol. 35, no. 2–4, pp. 211–219, 2007.
- [37] D. Yoshihiro and H. Yukio, "Crystal structures and magnetic properties of ordered perovskites Sr₂LnRuO₆ (Ln = Eu-Lu)," *J. Phys. Condens. Matter*, vol. 11, no. 25, pp. 4813–4820, 1999.
- [38] B. D. Cullity, *Elements of X-Ray Diffraction*, 1st ed. MASSACHUSETTS: ADDISON-WESLEY PUBLISHING COMPANY, Inc., 1956.
- [39] M. Srinivas, D. Modi, N. Patel, V. Verma, and K. V. R. Murthy, "Photoluminescence Studies and Core–Shell Model Approach for Rare Earthdoped CdWO₄ Nano Phosphor," *J. Inorg. Organomet. Polym. Mater.*, vol. 24, no. 6, pp. 988–993, Nov. 2014.
- [40] A. Boukerika and L. Guerbous, "Annealing effects on structural and luminescence properties of red Eu³⁺-doped Y₂O₃ nanophosphors prepared by sol – gel method," *J. Lumin.*, vol. 145, pp. 148–153, 2014.
- [41] M. Licheron, F. Gervais, J. Coutures, and J. Choynet, "'Ba₂BiO₄' surprisingly found as a cubic double perovskite," *Solid State Commun.*, vol. 75, no. 9, pp. 759–763, Sep. 1990.
- [42] R. Ratheesh, H. Sreemoolanadhan, and M. T. Sebastian, "Vibrational Analysis of Ba_{5-1-x}Sr_xNb₄O₁₅ Microwave Dielectric Ceramic Resonators," *Solid State Chem.*, vol. 8, no. 131, pp. 2–8, 1997.
- [43] L. J. T., "Infrared-Absorption Studies on Barium Titanate and Related Materials," *Phys. Rev.*, vol. 105, p. 1740, 1957.
- [44] B. E.J., "Structural chemistry and physicochemical properties of perovskite-like materials," *Catal. Today*, vol. 8, no. 2, pp. 133–151, 1990.

- [45] S. D. Ross, *Inorganic infrared and Raman spectra*. London; New York: McGraw-Hill, 1972.
- [46] A. E. Lavat, M. C. Grasselli, E. J. Baran, and R. C. Mercader, "Spectroscopic characterization of Ba LnSnO materials: 2 5.5 ceramic substrates for high T superconductors," *Mater. Letters*, vol. 47, no. 4–5, pp. 194–198, 2001.
- [47] A. Dutta and T. P. Sinha, "Dielectric Relaxation and Electronic Structure of Double Perovskite Ca₂AlNbO₆," *Integr. Ferroelectr.*, vol. 116, no. July 2015, pp. 41–50, 2010.
- [48] A. F. Corsmit, H. E. Hoefdraad, and G. Blasse, "Vibrational spectra of ordered perovskites," *J. Inorg. Nucl. Chem.*, vol. 34, no. 11, pp. 3401–3404, Nov. 1972.
- [49] G. Blasse and A. F. Corsmit, "Electronic and vibrational spectra of ordered perovskites," *J. Solid State Chem.*, vol. 6, no. 4, pp. 513–518, Apr. 1973.
- [50] W. S. Souza, R. O. Domingues, L. A. Bueno, E. B. Da Costa, and A. S. Gouveia-Neto, "Color tunable green-yellow-orange-red Er³⁺/Eu³⁺-codoped PbGeO₃:PbF₂:CdF₂ glass phosphor for application in white-LED technology," *J. Lumin.*, vol. 144, pp. 87–90, 2013.
- [51] W. Zheng, "Hydrothermal synthesis and characterization of perovskite-type Ba SbMO (M = In, Y, Nd) oxides," *Mater. Letters*, vol. 37, no. November, pp. 276–280, 1998.
- [52] P. Z. Zambare, A. P. Zambare, K. V. R. Murthy, and O. H. Mahajan, "Research Article Synthesis and Characterization of Red Emitting Sr₂CeO₄:Eu³⁺ Nano Phosphors," *J. Chem. Pharm. Res.*, vol. 4, no. 4, pp. 1990–1994, 2012.
- [53] D. K. Schroder, *Semiconductor Material and Device Characterization*, 3rd Editio. Hoboken, NJ, USA: John Wiley & Sons, Inc., 2005.
- [54] J. Andrés, V. Longo, L. Cavalcante, M. L. Moreira, J. Varela, and E. Longo, "A fresh look at the structural, ferroelectric and photoluminescent properties in perovskites," *Photoluminescence Appl. Types Effic.*, no. JANUARY, pp. 119–161, 2012.
- [55] A. Ohtomo and H. Y. Hwang, "A high-mobility electron gas at the LaAlO₃/SrTiO₃ heterointerface," *Nature*, vol. 427, no. 6973, pp. 423–426, Jan. 2004.
- [56] E. Longo *et al.*, "Density functional theory calculation of the electronic structure of Ba_{0.5}Sr_{0.5}TiO₃: Photoluminescent properties and structural disorder," *Phys.*

- Rev. B*, vol. 69, no. 12, p. 125115, Mar. 2004.
- [57] V. M. Longo *et al.*, “Structural conditions that leads to photoluminescence emission in SrTiO₃: An experimental and theoretical approach,” *J. Appl. Phys.*, vol. 104, no. 2, p. 023515, Jul. 2008.
- [58] R. I. Eglitis, E. A. Kotomin, V. A. Trepakov, S. E. Kapphan, and G. Borstel, “Quantum chemical modelling of electron polarons and green luminescence in PbTiO₃ perovskite crystals,” *J. Phys. Condens. Matter*, vol. 14, no. 39, pp. L647–L653, Oct. 2002.
- [59] I. W. Lenggoro, C. Panatarani, and K. Okuyama, “One-step synthesis and photoluminescence of doped strontium titanate particles with controlled morphology,” *Mater. Sci. Eng. B*, vol. 113, no. 1, pp. 60–66, Oct. 2004.
- [60] P. H. Borse, J. S. Lee, and H. G. Kim, “Theoretical band energetics of Ba(M_{0.5}Sn_{0.5})O₃ for solar photoactive applications,” *J. Appl. Phys.*, vol. 100, no. 12, p. 124915, Dec. 2006.
- [61] V. Petkov, M. Gateshki, M. Niederberger, and Y. Ren, “Atomic-Scale Structure of Nanocrystalline Ba_xSr_{1-x}TiO₃ (x = 1, 0.5, 0) by X-ray Diffraction and the Atomic Pair Distribution Function Technique,” *Chem. Mater.*, vol. 18, no. 3, pp. 814–821, Feb. 2006.
- [62] M.-L. Duan, X.-Y. Kuang, J.-H. Li, and Z.-Y. Jiao, “Theoretical study of local lattice structure of Mn²⁺ in perovskite fluorides A₂MF₄ (A=K, Rb; M=Mg, Zn, Cd) series,” *J. Phys. Chem. Solids*, vol. 68, no. 2, pp. 299–304, Feb. 2007.
- [63] L. S. Cavalcante *et al.*, “Combined experimental and theoretical investigations of the photoluminescent behavior of Ba(Ti,Zr)O₃ thin films,” *Acta Mater.*, vol. 55, no. 19, pp. 6416–6426, Nov. 2007.
- [64] A. T. de Figueiredo *et al.*, “Correlation among Order–Disorder, Electronic Levels, and Photoluminescence in Amorphous CT:Sm,” *Chem. Mater.*, vol. 18, no. 12, pp. 2904–2911, Jun. 2006.
- [65] V. M. Longo *et al.*, “Strong violet–blue light photoluminescence emission at room temperature in SrZrO₃: Joint experimental and theoretical study,” *Acta Mater.*, vol. 56, no. 10, pp. 2191–2202, Jun. 2008.
- [66] S. R. Phillpot, S. B. Sinnott, and A. Asthagiri, “Atomic-Level Simulation of Ferroelectricity in Oxides: Current Status and Opportunities,” *Annu. Rev. Mater. Res.*, vol. 37, no. 1, pp. 239–270, Aug. 2007.

- [67] S. G. Lu *et al.*, “Time-resolved photoluminescence of barium titanate ultrafine powders,” *J. Appl. Phys.*, vol. 99, no. 6, p. 064103, Mar. 2006.
- [68] H. Khassaf, J. V. Mantese, N. Bassiri-Gharb, Z. Kutnjak, and S. P. Alpay, “Pervoskite ferroelectrics and relaxor-ferroelectric solid solutions with large intrinsic electrocaloric response over broad temperature ranges,” *J. Mater. Chem. C*, vol. 4, no. 21, pp. 4763–4769, 2016.
- [69] S. A. Pauli and P. R. Willmott, “Conducting interfaces between polar and non-polar insulating pervoskites,” *J. Phys. Condens. Matter*, vol. 20, no. 26, p. 264012, Jul. 2008.
- [70] B. R. K. Nanda and S. Satpathy, “Effects of strain on orbital ordering and magnetism at pervoskite oxide interfaces: LaMnO₃ /SrMnO₃,” *Phys. Rev. B*, vol. 78, no. 5, p. 054427, Aug. 2008.
- [71] S. Okamoto, A. J. Millis, and N. A. Spaldin, “Lattice Relaxation in Oxide Heterostructures: LaTiO₃/SrTiO₃ Superlattices,” *Phys. Rev. Lett.*, vol. 97, no. 5, p. 056802, Jul. 2006.
- [72] X. Wu, M. Stengel, K. M. Rabe, and D. Vanderbilt, “Predicting Polarization and Nonlinear Dielectric Response of Arbitrary Pervoskite Superlattice Sequences,” *Phys. Rev. Lett.*, vol. 101, no. 8, p. 087601, Aug. 2008.
- [73] F. A. Urtiev, V. G. Kukhar, and N. A. Pertsev, “Phase diagrams of single-domain ferroelectric-dielectric superlattices,” *Appl. Phys. Lett.*, vol. 90, no. 25, p. 252910, Jun. 2007.
- [74] M. Sepliarsky, S. R. Phillpot, S. K. Streiffer, M. G. Stachiotti, and R. L. Migoni, “Polarization reversal in a pervoskite ferroelectric by molecular-dynamics simulation,” *Appl. Phys. Lett.*, vol. 79, no. 26, pp. 4417–4419, Dec. 2001.
- [75] M. L. Moreira, J. Andrés, V. M. Longo, M. S. Li, J. A. Varela, and E. Longo, “Photoluminescent behavior of SrZrO₃/SrTiO₃ multilayer thin films,” *Chem. Phys. Lett.*, vol. 473, no. 4–6, pp. 293–298, May 2009.
- [76] M. L. Moreira, J. Andrés, J. A. Varela, and E. Longo, “Synthesis of Fine Micro-sized BaZrO₃ Powders Based on a Decaohedron Shape by the Microwave-Assisted Hydrothermal Method,” *Cryst. Growth Des.*, vol. 9, no. 2, pp. 833–839, Feb. 2009.
- [77] L. S. Cavalcante *et al.*, “Experimental and theoretical correlation of very intense visible green photoluminescence in BaZrO₃ powders,” *J. Appl. Phys.*, vol. 103,

- no. 6, p. 063527, Mar. 2008.
- [78] G.-C. Yi, B. A. Block, G. M. Ford, and B. W. Wessels, "Luminescence quenching in Er-doped BaTiO₃ thin films," *Appl. Phys. Lett.*, vol. 73, no. 12, pp. 1625–1627, Sep. 1998.
- [79] J. Yu, J. Chu, and M. Zhang, "Syntheses of nanocrystalline BaTiO₃ and their optical properties," *Appl. Phys. A Mater. Sci. Process.*, vol. 74, no. 5, pp. 645–647, May 2002.
- [80] C. D. Pinheiro *et al.*, "The role of defect states in the creation of photoluminescence in SrTiO₃," *Appl. Phys. A Mater. Sci. Process.*, vol. 77, no. 1, pp. 81–85, Jun. 2003.
- [81] L. E. B. Soledade *et al.*, "Room-temperature photoluminescence in amorphous SrTiO₃ - the influence of acceptor-type dopants," *Appl. Phys. A Mater. Sci. Process.*, vol. 75, no. 5, pp. 629–632, Nov. 2002.
- [82] W. F. Zhang, Z. Yin, M. S. Zhang, Z. L. Du, and W. C. Chen, "Roles of defects and grain sizes in photoluminescence of nanocrystalline SrTiO₃," *J. Phys. Condens. Matter*, vol. 11, no. 29, pp. 5655–5660, Jul. 1999.
- [83] P. S. Pizani *et al.*, "Photoluminescence of disordered ABO₃ perovskites," *Appl. Phys. Lett.*, vol. 77, no. 6, pp. 824–826, Aug. 2000.
- [84] J. Yu, J. Sun, J. Chu, and D. Tang, "Light-emission properties in nanocrystalline BaTiO₃," *Appl. Phys. Lett.*, vol. 77, no. 18, pp. 2807–2809, Oct. 2000.
- [85] M. C. F. Alves *et al.*, "Influence of the modifier on the short and long range disorder of stannate perovskites," *J. Alloys Compd.*, vol. 476, no. 1–2, pp. 507–512, May 2009.
- [86] H. Mizoguchi, P. M. Woodward, C.-H. Park, and D. A. Keszler, "Strong Near-Infrared Luminescence in BaSnO₃," *J. Am. Chem. Soc.*, vol. 126, no. 31, pp. 9796–9800, Aug. 2004.
- [87] A. T. de Figueiredo *et al.*, "Blue-green and red photoluminescence in CaTiO₃:Sm," *J. Lumin.*, vol. 126, no. 2, pp. 403–407, Oct. 2007.
- [88] L. L.D., "Über Die Bewegung der Elektronen in Kristallgitter," *Phys. Z. Sowjetunion*, vol. 3, pp. 644–645, 1933.
- [89] R. Leonelli and J. L. Brebner, "Time-resolved spectroscopy of the visible emission band in strontium titanate," *Phys. Rev. B*, vol. 33, no. 12, pp. 8649–8656, Jun. 1986.

- [90] J. Meng, Y. Huang, W. Zhang, Z. Du, Z. Zhu, and G. Zou, “Photoluminescence in nanocrystalline BaTiO₃ and SrTiO₃,” *Phys. Lett. A*, vol. 205, no. 1, pp. 72–76, Sep. 1995.
- [91] V. S. Vikhnin, R. I. Eglitis, S. E. Kapphan, E. A. Kotomin, and G. Borstel, “A new phase in ferroelectric oxides: The phase of charge transfer vibronic excitons,” *Europhys. Lett.*, vol. 56, no. 5, pp. 702–708, Dec. 2001.
- [92] V. S. Vikhnin, A. A. Kaplyanskii, A. B. Kutsenko, G. K. Liu, J. V. Beitz, and S. E. Kapphan, “‘Charge transfer–lattice’ clusters induced by charged impurities,” *J. Lumin.*, vol. 94–95, pp. 775–779, Dec. 2001.
- [93] E. Orhan *et al.*, “Room-temperature photoluminescence of BaTiO₃: Joint experimental and theoretical study,” *Phys. Rev. B*, vol. 71, no. 8, p. 085113, Feb. 2005.
- [94] Y. Kawabe *et al.*, “Photoluminescence of perovskite lanthanum aluminate single crystals,” *J. Appl. Phys.*, vol. 87, no. 10, pp. 7594–7596, May 2000.
- [95] E. Orhan *et al.*, “Combined Experimental and Theoretical Study to Understand the Photoluminescence of Sr_{1-x}TiO_{3-x},” *J. Phys. Chem. B*, vol. 108, no. 26, pp. 9221–9227, Jul. 2004.
- [96] E. R. Leite *et al.*, “The origin of photoluminescence in amorphous lead titanate,” *J. Mater. Sci.*, vol. 38, no. 6, pp. 1175–1178, 2003.
- [97] E. R. Leite *et al.*, “Photoluminescence of nanostructured PbTiO₃ processed by high-energy mechanical milling,” *Appl. Phys. Lett.*, vol. 78, no. 15, pp. 2148–2150, Apr. 2001.
- [98] M. Anicete-Santos *et al.*, “Contribution of structural order–disorder to the room-temperature photoluminescence of lead zirconate titanate powders,” *J. Lumin.*, vol. 127, no. 2, pp. 689–695, Dec. 2007.
- [99] N. Bloembergen, “Solid State Infrared Quantum Counters,” *Phys. Rev. Lett.*, vol. 2, no. 3, pp. 84–85, Feb. 1959.
- [100] H. Gobrecht, “Über die Absorptions- und Fluoreszenzspektren der Ionen der Seltenen Erden in festen Körpern, insbesondere im Ultrarot,” *Ann. Phys.*, vol. 420, no. 8, pp. 673–700, 1937.
- [101] M. P. Hehlen, M. G. Brik, and K. W. Krämer, “50th anniversary of the Judd–Ofelt theory: An experimentalist’s view of the formalism and its application,” *J. Lumin.*, vol. 136, pp. 221–239, Apr. 2013.

- [102] B. M. Walsh, “Judd-Ofelt theory: principles and practices,” in *Advances in Spectroscopy for Lasers and Sensing*, Dordrecht: Springer Netherlands, 2006, pp. 403–433.
- [103] R. D. Peacock, “The intensities of lanthanide $f \leftrightarrow f$ transitions,” in *Rare Earths*, Berlin, Heidelberg: Springer Berlin Heidelberg, pp. 83–122.
- [104] G. S. Ofelt, “Intensities of Crystal Spectra of Rare-Earth Ions,” *J. Chem. Phys.*, vol. 37, no. 3, pp. 511–520, Aug. 1962.
- [105] B. R. Judd, “Optical Absorption Intensities of Rare-Earth Ions,” *Phys. Rev.*, vol. 127, no. 3, pp. 750–761, Aug. 1962.
- [106] C. Görller-Walrand and K. Binnemans, “Spectral intensities of f-f transitions,” in *Handbook on the Physics and Chemistry of Rare Earths*, Elsevier, 1998, pp. 101–264.
- [107] C. Görller-Walrand, L. Fluyt, A. Ceulemans, and W. T. Carnall, “Magnetic dipole transitions as standards for Judd–Ofelt parametrization in lanthanide spectra,” *J. Chem. Phys.*, vol. 95, no. 5, pp. 3099–3106, Sep. 1991.
- [108] S. K. Sekatskii and G. Dietler, “Using Magnetic Dipole Transitions for Fluorescence Resonance Energy Transfer,” *Anal. Biochem.*, vol. 299, no. 2, pp. 263–266, Dec. 2001.
- [109] K. Binnemans, “Interpretation of europium(III) spectra,” *Coord. Chem. Rev.*, vol. 295, pp. 1–45, Jul. 2015.
- [110] H. E. Hoefdraad, “The charge-transfer absorption band of Eu^{3+} in oxides,” *J. Solid State Chem.*, vol. 15, no. 2, pp. 175–177, Oct. 1975.
- [111] V. Sivakumar and U. V. Varadaraju, “Synthesis, phase transition and photoluminescence studies on Eu^{3+} -substituted double perovskites—A novel orange-red phosphor for solid-state lighting,” *J. Solid State Chem.*, vol. 181, no. 12, pp. 3344–3351, Dec. 2008.
- [112] Y. Zhang, J. Xu, Q. Cui, and B. Yang, “ Eu^{3+} -doped $\text{Bi}_4\text{Si}_3\text{O}_{12}$ red phosphor for solid state lighting: microwave synthesis, characterization, photoluminescence properties and thermal quenching mechanisms,” *Sci. Rep.*, vol. 7, no. 1, p. 42464, Mar. 2017.
- [113] G. Blasse and B. C. Grabmaier, *Luminescent Materials*. Berlin, Heidelberg: Springer Berlin Heidelberg, 1994.
- [114] M. Ayvacıklı, A. Ege, S. Yerci, and N. Can, “Synthesis and optical properties of

- Er³⁺ and Eu³⁺ doped SrAl₂O₄ phosphor ceramic,” *J. Lumin.*, vol. 131, no. 11, pp. 2432–2439, Nov. 2011.
- [115] Y.-H. Won, H. S. Jang, W. Bin Im, and D. Y. Jeon, “Red-Emitting LiLa₂O₂BO₃:Sm³⁺,Eu³⁺ Phosphor for Near-Ultraviolet Light-Emitting Diodes-Based Solid-State Lighting,” *J. Electrochem. Soc.*, vol. 155, no. 9, p. J226, 2008.
- [116] P. Ptacek, H. Schäfer, K. Kömpe, and M. Haase, “Crystal Phase Control of Luminescing α -NaGdF₄:Eu³⁺ and β -NaGdF₄:Eu³⁺ Nanocrystals,” *Adv. Funct. Mater.*, vol. 17, no. 18, pp. 3843–3848, Dec. 2007.
- [117] S. Y. Kim, Y.-H. Won, and H. S. Jang, “A Strategy to enhance Eu³⁺ emission from LiYF₄:Eu nanophosphors and green-to-orange multicolor tunable, transparent nanophosphor-polymer composites,” *Sci. Rep.*, vol. 5, no. 1, p. 7866, Jul. 2015.
- [118] F. M. Emen and R. Altinkaya, “Luminescence and thermoluminescence properties of Sr₃WO₆:Eu³⁺ phosphor,” *J. Lumin.*, vol. 134, pp. 618–621, Feb. 2013.
- [119] Y. Shimada, H. Kiyama, and Y. Tokura, “Magnetoelectric emission in rare-earth doped ferroelectric crystals La₂Ti₂O₇:R³⁺ (R=Er, Eu, and Nd),” *Phys. Rev. B*, vol. 75, no. 24, p. 245125, Jun. 2007.
- [120] G. B. F. Bosco and L. R. Tessler, “Crystal field parameters of the C₂ site in Eu₂O₃,” *Opt. Mater. X*, vol. 2, p. 100028, May 2019.
- [121] S. Zhang, Y. Hu, L. Chen, X. Wang, G. Ju, and Y. Fan, “Photoluminescence properties of Ca₃WO₆:Eu³⁺ red phosphor,” *J. Lumin.*, vol. 142, pp. 116–121, Oct. 2013.
- [122] X. Zhao, Y. Ding, Z. Li, T. Yu, and Z. Zou, “An efficient charge compensated red phosphor Sr₃WO₆: K⁺, Eu³⁺ – For white LEDs,” *J. Alloys Compd.*, vol. 553, pp. 221–224, Mar. 2013.
- [123] X. Zhao *et al.*, “Efficient red phosphor double-pervoskite Ca₃WO₆ with A-site substitution of Eu³⁺,” *Dalt. Trans.*, vol. 42, no. 37, p. 13502, 2013.
- [124] K. V. Dabre, K. Park, and S. J. Dhoble, “Synthesis and photoluminescence properties of microcrystalline Sr₂ZnWO₆:RE³⁺ (RE = Eu, Dy, Sm and Pr) phosphors,” *J. Alloys Compd.*, vol. 617, pp. 129–134, Dec. 2014.
- [125] A. Huignard, T. Gacoin, and J.-P. Boilot, “Synthesis and Luminescence

- Properties of Colloidal YVO₄:Eu Phosphors,” *Chem. Mater.*, vol. 12, no. 4, pp. 1090–1094, Apr. 2000.
- [126] J. McKittrick and L. E. Shea-Rohwer, “Review: Down Conversion Materials for Solid-State Lighting,” *J. Am. Ceram. Soc.*, vol. 97, no. 5, pp. 1327–1352, May 2014.
- [127] A. Fu *et al.*, “A novel double perovskite La₂ZnTiO₆:Eu³⁺ red phosphor for solid-state lighting: Synthesis and optimum luminescence,” *Opt. Laser Technol.*, vol. 96, pp. 43–49, Nov. 2017.
- [128] S. Sheoran, V. Singh, S. Singh, S. Kadyan, J. Singh, and D. Singh, “Down-conversion characteristics of Eu³⁺ doped M₂Y₂Si₂O₉ (M = Ba, Ca, Mg and Sr) nanomaterials for innovative solar panels,” *Prog. Nat. Sci. Mater. Int.*, vol. 29, no. 4, pp. 457–465, Aug. 2019.
- [129] G. Lin *et al.*, “Three primary colors emitting from Er³⁺–Eu³⁺ co-doped oxygen-deficient glasses,” *J. Alloys Compd.*, vol. 509, no. 22, pp. 6462–6466, Jun. 2011.
- [130] N. Jain *et al.*, “Synthesis and Rational design of Europium and Lithium Doped Sodium Zinc Molybdate with Red Emission for Optical Imaging,” *Sci. Rep.*, vol. 9, no. 1, p. 2472, Dec. 2019.
- [131] Y. Gao *et al.*, “Tb³⁺ and Eu³⁺ co-doped Ba₆Bi₉B₇₉O₁₃₈: color-tunable phosphors by utilizing the host-sensitization effect of Bi³⁺ and enhancement of red emission upon heating,” *New J. Chem.*, vol. 41, no. 5, pp. 2037–2045, 2017.
- [132] A. Katelnikovas, H. Winkler, A. Kareiva, and T. Jüstel, “Synthesis and optical properties of green to orange tunable garnet phosphors for pcLEDs,” *Opt. Mater. (Amst.)*, vol. 33, no. 7, pp. 992–995, May 2011.
- [133] D. Chen, Y. Wang, Y. Yu, P. Huang, and F. Weng, “Novel rare earth ions-doped oxyfluoride nano-composite with efficient upconversion white-light emission,” *J. Solid State Chem.*, vol. 181, no. 10, pp. 2763–2767, Oct. 2008.
- [134] J. S. Zhong, H. B. Gao, Y. J. Yuan, L. F. Chen, D. Q. Chen, and Z. G. Ji, “Eu³⁺-doped double perovskite-based phosphor-in-glass color converter for high-power warm w-LEDs,” *J. Alloys Compd.*, vol. 735, pp. 2303–2310, Feb. 2018.
- [135] J. Zheng, Q. Cheng, C. Zheng, G. Chen, F. Shi, and C. Chen, “Correlated color temperature tunability and energy transfer phenomenon in the NaBaBO₃:Dy³⁺/Eu³⁺ phosphor for white light application,” *Funct. Mater. Lett.*, vol. 08, no. 06, p. 1550077, Dec. 2015.

- [136] Y. Wei *et al.*, “Emitting-tunable Eu (2+/3+) -doped Ca (8-x) La (2+x) (PO₄)_{6-x} (SiO₄)_x O₂ apatite phosphor for n-UV WLEDs with high-color-rendering,” *RSC Adv.*, vol. 7, no. 4, pp. 1899–1904, 2017.